Flow of a shallow film over a moving surface

X. Liu (刘小禾),[1] S. Green,[1] B. Stoeber,[1] and Neil J. Balmforth[2, a)]
[1)] *Department of Mechanical Engineering, University of British Columbia, Vancouver, BC, V6T 1Z4, Canada*
[2)] *Department of Mathematics, University of British Columbia, Vancouver, BC, V6T 1Z2, Canada*

The von-Karman-Pohlhausen averaging technique is employed to build a reduced model for the flow of a shallow film from a sluice gate or impacting jet over a moving surface. The viscous drag exerted on the film by the moving wall acts to arrest flow counter to the direction of the wall's motion, and force an adjustment towards the wall speed. For a (normally) impacting jet, this results in a range of wall speeds for which a steady state is reached in which all the fluid is eventually recirculated to flow along the wall, with a distinctive "heel" forming upstream of the impact region. For wall speeds below this range, the flow counter to the wall cannot be arrested, and unsteady states result. For wall speeds above this range, a different steady state emerges in which fluid is immediately diverted through and downstream of the impact region, eliminating any heel. The steady, heeled flow states predicted by the reduced model are in qualitative agreement with numerical simulations of the full two-dimensional problem.

I. INTRODUCTION

The impact of a high-speed jet on to a surface creates a spreading, shallow fluid film that is familiar from a host of everyday settings. In some situations, the outflowing film meets a hydraulic jump, and a vein of previous literature has been aimed at rationalizing the location and structure of that sudden change in depth (*e.g.* Refs. 2–4, 7, and 20). The impact of a jet on an inclined or vertical surface has also been of interest[1,9,19]. Here, we consider a different aspect of the problem, namely the dynamics of the spreading films generated by the impact of a jet onto a moving surface. This version of the impingement problem has been explored for circular jets on moving planes, partly with the applications of cooling or cleaning surfaces in mind (*e.g.* Refs. 5, 6, 16, 21–23). The current discussion considers the corresponding two-dimensional configuration, which is more like that arising near impingement in the curtain coating process[15].

Although there is some interest in the detailed dynamics in the vicinity of the area of impingement, the high impact pressures that are generated there abruptly divert the incoming fluid into films spreading in either direction along the wall. We focus primarily on those spreading films, relegating our discussion of the impact zone to a relatively crude treatment. The novelty of the moving wall derives from the effect on these films: where the film spreads in the direction of the wall's motion, a viscous boundary layer is expected to develop that accelerates or brakes the film so that it reaches the wall speed. The development of the boundary layer on the other side, however, inevitably slows the outflow, causing fluid to pile up. The slowed fluid may then be carried back underneath the outflowing film and jet. A key issue is whether the wall motion thereby arrests the spreading of fluid in that one direction, leading to a steady state in which all the fluid is eventually recirculated back in the direction of the wall. Alternatively, it may be possible that the fluid continues to spread counter to the wall motion, piling up in depth all the while. Part of our goal is to explore this issue and to map out the flow dynamics in detail. Although the detailed fluid dynamics and the resolution of this key issue depend critically on the two-dimensional nature of the problem, one still envisions that some aspects may bear on the more practical problem of the three-dimensional impact of a circular jet on a moving plane.

Our analysis proceeds by exploiting the shallowness of the spreading films and using boundary-layer theory. In particular, we use the von Karman-Pohlhausen averaging scheme to develop shallow layer equations for the film. Unlike many conventional approaches, we consider the time-dependent version of the boundary-layer analysis in order to avoid the awkward possibility that no steady state exists. The averaging scheme allows us to capture the almost inviscid currents diverted from the jet as well as the viscous boundary layer underneath. The theory accounts for the incoming mass and impact pressures from the jet using the relatively simple, but crude, device of adding prescribed sources of mass and momentum to the shallow-layer equations. Although the approximations that we employ in the analysis are therefore relatively rough, they lead to a simple model that allows us to take the first steps in interrogating the complexities of the impingement problem with a moving wall. As an alternative, one might try to avoid the von Karman-Pohlhausen averaging, and use the full boundary-layer equations, as has been done for steady jet impingement on stationary or rotating surfaces[2,7,18]. However, incorporating the effects of unsteadiness and the counter flow induced by the moving wall renders such an approach more challenging. Awkwardly, the boundary-layer equations also do not remain valid over the relatively small scale of the impact zone, demanding a match to a separate solution for this finer region (e.g. Ref. 18), the

[a)] Electronic mail: njb@math.ubc.ca.

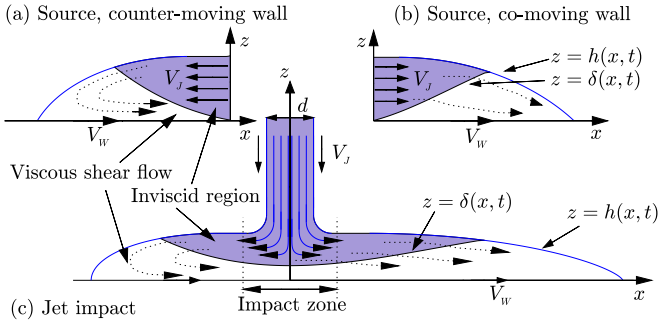

FIG. 1. Sketch of the model geometries considered for the boundary-layer theory. In (a) and (b), fluid moves through a gate at $x = 0$ with uniform horizontal speed V_J on to a surface travelling at speed V_W. In (c), a uniform jet impacts the moving wall instead.

transparency of which is again obscured by unsteadiness and counter flow.

We pave our way to the two-dimensional (slot) jet problem by first considering two simpler problems without the complication of an impact region: when the wall is stationary, the outflows to the left and right are symmetrical, each being similar to that formed from an outflow from a sluice gate (*i.e.* a line source of momentum with a prescribed depth). This is the analogue of the two-dimensional problem considered by Watson[20], although he considered only the steady state in which a hydraulic jump appeared further from the source due to downstream effects. By contrast, as a first problem, we consider the time-dependent version of Watson's configuration in which the outflow advances over the plane in the manner of a gravity current (although we ignore gravity). The impact zone underneath the jet is thereby replaced by a suitable boundary condition. To understand the spreading characteristics, we draw inspiration from literature on spreading flows described by Saint-Venant-type equations[8]. Our second problem adds a moving wall to this problem of a time-dependent outflow from a source, allowing the fluid to be directed in the same sense or opposite to the motion of the wall. These two problems provide convenient building blocks in understanding the full jet problem.

Finally, we compare the results of the boundary-layer theory with simulations of the full two-dimensional problem. As the averaging theory is not based on any true asymptotic reduction, the best one may hope for in such a comparison is qualitative agreement. Indeed, we find that a number of the detailed results predicted by the boundary-layer analysis are borne out by the numerical computations.

II. TIME-DEPENDENT BOUNDARY LAYER THEORY

A. Model formulation

As sketched in figure 1, we consider the flow of a two-dimensional, shallow film of incompressible fluid over a planar moving surface. The fluid is introduced onto the plane either from a line source (mimicking a sluice gate) or an impacting jet. The geometry is described using a Cartesian coordinate system (x, z) in which the plane is located along $z = 0$ and moves with speed V_W in the positive $x-$direction. In the first configuration (figure 1(a,b)), the line source lies at the origin, and directs fluid of a prescribed depth either to the right or left with a horizontal velocity of $\pm V_J$. For the second (figure 1(c)), the central axis of the jet is aligned with the $z-$axis and we take the incoming fluid to have uniform speed V_J and width d.

In the boundary-layer approximation, the governing equations of mass and momentum conservation for a two-dimensional incompressible fluid film take the form,

$$u_x + w_z = 0, \tag{1}$$

$$u_t + uu_x + wu_z = -\rho^{-1}p_x + \nu u_{zz}, \tag{2}$$

$$0 = -\rho^{-1}p_z, \tag{3}$$

where $(u(x,z,t), w(x,z,t))$ denotes the velocity field, $p(x,z,t)$ is the pressure, ρ is the density, ν denotes the kinematic viscosity, and we have ignored gravity. We denote the top surface of the film by $h(x,t)$; in the absence of surface tension, the kinematic and stress conditions on this free surface demand

$$\left.\begin{array}{r} h_t + uh_x = w \\ p = 0,\ u_z = 0 \end{array}\right\} \text{ on } z = h(x,t). \tag{4}$$

1. Line sources

To model a line source we imagine that there is a gate of height $\frac{1}{2}d$ through which the fluid moves uniformly at speed V_J. Thus, there is horizontal flux of $\frac{1}{2}dV_J$ at $x = 0$. When Reynolds numbers are relatively high, a viscous boundary layer forms at the bottom of the film flowing out from the source. With distance, this layer diffuses up through the fluid, adjusting flow speeds towards the wall speed in the case that the source directs flow to the right, or slowing the fluid to prompt a pile up of the fluid when the source directs flow to the left. If we denote the thickness of the viscous boundary layer by $\delta(x,t)$, the boundary conditions to impose at the source are

$$\left.\begin{array}{r} h = \frac{1}{2}d \\ u = \pm V_J \\ \delta = 0 \end{array}\right\} \text{ at } x = 0. \tag{5}$$

Further from the source, the viscous boundary layer consumes the plug-like outflow from the source to furnish

$\delta(x,t) = h(x,t)$. The top surface speed $u(x,h,t)$ then no longer matches $\pm V_J$, leaving a fully developed shear flow; *cf.* figure 1(a,b). Note that the first boundary condition in (5) precludes any backflow from reaching to the gate, a feature that can lead to inconsistencies, as we mention later.

2. The impact zone underneath the jet

The impact of the jet with the moving wall generates a pressure that sharply diverts the uniform downflow into shallow films that spread largely horizontally in either direction. The zone where impact pressures are high occupies a region of scale d around the origin, and the diverging flow here is largely unaffected by viscosity. Only over a much longer horizontal scale L do viscous effects come into play to control spreading. The diverging flow over the impact zone is therefore close to potential flow[10,11]. However, unlike for a stationary surface, fluid spreading against the motion of the wall can be viscously arrested and then carried back underneath the impacting jet, elevating the incoming potential flow above the returning layer and complicating the possible flow patterns (see figure 1(c)).

Directly underneath the jet, fluid rains down at speed V_J into the film and there is no free surface. We nevertheless continue to identify the level $z = h(x,t)$ as the upper surface of the film, supplementing the kinematic condition there with the mass flux from the jet:

$$h_t + uh_x = w + V_J \Theta\left(\tfrac{1}{2}d - |x|\right) \quad \text{on} \quad z = h(x,t). \quad (6)$$

where $\Theta(x)$ denotes Heaviside's step function.

The jet also adds a source of horizontal momentum to the film through the gradient of the impact pressure. In particular, over a distance of order d, the impact pressure diverts the incoming flow sideways to spread at speed V_J. We account for this crudely by setting

$$p_x = -\rho {V_J}^2 \frac{\mathrm{d}}{\mathrm{d}x}\left(\tfrac{1}{2}{u_I}^2\right), \quad (7)$$

where $u_I(x)$ denotes the local horizontal speed to which the impact pressure drives the fluid, scaled by the jet speed. Practically, we adopt the simple model

$$u_I = \tanh\frac{\alpha x}{d}, \quad (8)$$

which provides an impact pressure that matches that observed in the numerical simulations of the full two-dimensional problem reported in §V for $\alpha \approx 1$ (the value we adopt below).

These depth-independent side flows from the jet sit above fluid that is slowed or redirected by the viscous interaction with the moving wall. Thus, one anticipates that, at least to begin with, there is a superficial layer of fluid in the neighbourhood of the impact zone that moves at speed $V_J u_I(x)$, overlying a viscous shear flow. As before, we take the sheared viscous region to have thickness $\delta(x,t)$, so that the overlying, nearly inviscid flow with $u(x,z,t) = V_J u_I(x)$ occupies $\delta < z < h$. Again, this plug-like sideways flow becomes consumed by the viscous layer sufficiently far from the impact zone (furnishing $\delta(x,t) = h(x,t)$), to either leave a fully developed shear flow or redirect all the fluid into the direction of the wall; *cf.* figure 1(c).

B. Reduction

1. $\delta(x,t) < h(x,t)$

Where the film possesses a superficial inviscid flow, the upper fluid has flow speed $u(x,h,t) = V_J u_T(x,t) = V_J u_I(x)$, where u_T is the upper fluid's y-velocity component as a function of x and t, and $u_I = \pm 1$ for the line source, or is generated by the impact pressure gradient *via* (7)–(8) for the jet. In either case, we then approximate the full vertical profile of the horizontal velocity by

$$u(x,z,t) = V_J \times \begin{cases} u_W + Uf(\zeta), & 0 \le z \le \delta, \\ u_T, & \delta \le z \le h. \end{cases}, \quad (9)$$

where

$$U = u_T - u_W, \quad \zeta = \frac{z}{\delta}, \quad u_W = \frac{V_W}{V_J}. \quad (10)$$

For the moment, we leave open the choice for the profile function, which satisfies

$$f(0) = f'(1) = 0, \quad f(1) = 1, \quad f'(0) = c_0, \quad (11)$$

$$c_j = \int_0^1 [f(\zeta)]^j \mathrm{d}\zeta \quad (j \neq 0), \quad (12)$$

for some constants c_0, c_1 and c_2. Later, however, we adopt the simple parabola $f(\zeta) = \zeta(2-\zeta)$, implying $c_0 = 2$, $c_1 = \frac{2}{3}$ and $c_2 = \frac{8}{15}$. Other choices are possible, with higher order polynomials useful in imposing additional constraints in the boundary-layer theory. However, as discussed by Majdalani & Xuan[14], the relatively simple parabolic profile offers a useful first choice.

The depth integral of the continuity equation (1), in conjunction with the kinematic condition (6) now furnishes

$$h_t + V_J(u_W h + q)_x = V_J \Theta\left(\tfrac{1}{2}d - |x|\right), \quad (13)$$

where we write the material flux as

$$\int_0^h u \, \mathrm{d}z = V_J\left(u_W h + q\right), \quad (14)$$

which in view of the profile (9), must also equal $V_J[u_W h + Uc_1\delta + U(h-\delta)]$, and so

$$q \equiv U[h - (1-c_1)\delta]. \quad (15)$$

Given that (2) may be rewitten as

$$(u-V_{J}u_{I})_t+[u(u-V_{J}u_{I})]_x+[w(u-V_{J}u_{I})]_z \\ +V_{J}(u-V_{J}u_{I})u_{I}{}'=\nu u_{zz}, \tag{16}$$

an integral of the momentum equation over the sheared region also provides

$$(c_1-1)U\delta_t+V_{J}[u_wU(c_1-1)\delta+U^2(c_2-c_1)\delta]_x+ \\ +V_{J}u_{I}{}'U(c_1-1)\delta=-\frac{\nu u_z(x,0,t)}{V_{J}}=-\frac{\nu c_0U}{\delta}. \tag{17}$$

After a little algebra, and in conjunction with (13) and (15), this relation may be turned into an evolution equation for the variable q:

$$q_t+V_{J}\left[U(u_{I}h-V\delta)\right]_x=-\nu c_0\frac{U}{\delta} \\ +V_{J}\left[hu_{I}u_{I}{}'+U\Theta\left(\tfrac{1}{2}d-|x|\right)\right], \tag{18}$$

where

$$V=u_{I}(1-c_2)+u_{W}(c_2-c_1). \tag{19}$$

2. $\delta(x,t)=h(x,t)$

Once the viscous boundary layer consumes the entire film, the top horizontal velocity $u_{T}(x,t)$ is no longer equal to $u_{I}(x)$, and instead of (9) we have

$$u(x,z,t)=V_{J}[u_{W}+Uf(\zeta)],\quad \zeta=\frac{z}{h}. \tag{20}$$

If we now set

$$q=c_1hU=c_1h(u_{T}-u_{W}), \tag{21}$$

the material flux is still (14), leaving the depth-integrated mass conversation in the form (13). The depth-integral of the momentum equation now gives

$$q_t+V_{J}\left(u_wq+\frac{c_2q^2}{c_1^2h}\right)_x=-\frac{\nu c_0q}{c_1h^2} \\ +V_{J}\left[hu_{I}u_{I}{}'+\frac{q}{c_1h}\Theta\left(\tfrac{1}{2}d-|x|\right)\right]. \tag{22}$$

C. Dimensionless model

We remove dimensions from the model equations by defining the scaled variables,

$$(\hat{h},\hat{\delta},\hat{q})=\frac{2}{d}(h,\delta,q),\quad \hat{t}=\frac{V_{J}}{L}t,\quad \hat{x}=\frac{x}{L}, \tag{23}$$

where the horizontal lengthscale is given by

$$L=\frac{c_1V_{J}d^2}{4c_0\nu}=\tfrac{1}{2}d\,\mathrm{Re}_{J}\frac{c_1}{2c_0},\quad \mathrm{Re}_{J}=\frac{V_{J}d}{\nu}, \tag{24}$$

and Re_{J} is the Reynolds number. For the jet, the width then becomes $-x_s<x<x_s$, with

$$x_s=\frac{d}{2L}\equiv\frac{2c_0}{c_1\mathrm{Re}_{J}}, \tag{25}$$

and the dimensionless model equations, after dropping the hat decoration, can be written compactly as

$$h_t+u_{W}h_x+q_x=S, \\ q_t+M_x=hu_{I}u_{I}{}'+US-\frac{c_1U}{\delta}, \tag{26}$$

where

$$\delta=\mathrm{Min}\left(h,\frac{Uh-q}{U(1-c_1)}\right),\qquad U=u_{T}-u_{W}, \\ M=\begin{cases}u_{W}q+\dfrac{c_2q^2}{c_1^2h}, & h=\delta\ \ (u_{T}=u_{W}+\dfrac{q}{c_1h}\neq u_{I}),\\ U\left(u_{I}h-V\delta\right), & h>\delta\ \ (u_{T}=u_{I}),\end{cases} \\ u_{I}=\tanh\left(\frac{\alpha x}{2x_s}\right),\qquad S(x)=\frac{1}{x_s}\Theta(x_s-|x|). \\ V=u_{I}(1-c_2)+u_{W}(c_2-c_1). \tag{27}$$

The equations for line sources are similar, except that we set $S=0$ and $u_{I}=\pm1$, and impose the boundary conditions, $h(0,t)=1$ and $q(0,t)=U=u_{I}-u_{W}$ (or $\delta(0,t)=0$).

We solve the model equations numerically as an initial-value problem by placing a grid on a finite computational domain with $0<|x|<L_2$ or $-L_1<x<L_2$. We assume that $h=\delta=h_\infty$ and $q=0$ for $x<-L_1$ and $x>L_2$, and adopt initial conditions with $h\geq h_\infty$ everywhere, with $h_\infty>0$ a small parameter characterizing a thin pre-wetted film. We then discretize spatial derivatives using the first or second-order schemes of Kurgansky & Tadmor (2000), and solve the resulting set of coupled ODEs using MATLAB's ODE15s. Practically, we take $h_\infty=10^{-2}$ or less, and use a grid of 800 or 1600 points. Prewetting the moving wall in this fashion avoids any need to explicitly consider the moving free boundaries at the front and back edges of the fluid, $x=x_{f,b}(t)$, where $(h,q)\to0$. Instead, we define these edges as the locations where $h=2.5\times h_\infty$. By changing the value of h_∞, we have confirmed that this parameter does not play a major role in the dynamics.

Note that, in principle, the relative shallowness of the film (or equivalently high Reynolds number) implies that we should take the width of the jet to have $x_s=d/(2L)\ll1$ (the vertical scale is $O(d)$, whereas L provides a characteristic horizontal lengthscale). In practice, we relax this constraint somewhat, allowing the impact zone to be somehat small, but not especially so, in order to have some resolution of this region within the boundary-layer framework.

As remarked earlier, in all the examples we present below, we choose the profile constants $c_0=2$, $c_1=\frac{2}{3}$ and $c_2=\frac{8}{15}$, and set $\alpha=1$ for the impact pressure distribution. The key remaining dimensionless parameters are

the velocity ratio $u_{_W}$ (dimensionless wall speed) and the jet width x_s (or, equivalently, the Reynolds number; see (25)).

III. LINE SOURCES

A. Stationary wall ($\mathbf{u_w = 0}$, $\mathbf{x_s \to 0}$)

We first retire to Watson's problem and consider a stationary wall. In this setting, the outflow is left-right symmetrical, so we simplify the problem by shrinking the impact zone to a point, $x_s \to 0$, and launching a uniform flow from the origin with depth $h(0,t) = 1$ and flux $q(0,t) = 1$ ($\delta(0,t) = 0$). The model equations simplify to

$$h_t + q_x = 0, \qquad \delta = \text{Min}\left(h, \frac{h-q}{1-c_1}\right). \tag{28}$$

$$\begin{cases} q_t + \left(\dfrac{c_2 q^2}{c_1^2 h}\right)_x = -\dfrac{q}{h^2}, \quad \delta = h \qquad \left(u_{_T} = \dfrac{q}{c_1 h}\right), \\ q_t + \left[h - (1-c_2)\delta\right]_x = -\dfrac{c_1}{\delta}, \quad \delta < h \quad (u_{_T} = 1). \end{cases} \tag{29}$$

A numerical solution to this set of equations is shown in figure 2. The outflow creates a fluid step that travels to the right with a speed close to $t^{\frac{1}{2}}$, and leaves behind a steady state.

The steady solution to the rear has constant flux $q = 1$, and the profile

$$\delta = \sqrt{\frac{2c_1 x}{c_1 - c_2}}, \quad h = 1 + (1-c_1)\delta, \quad u_{_T} = 1 \tag{30}$$

for $x < (c_1 - c_2)/(2c_1^3)$, and

$$h = \delta = \frac{3c_2 - c_1}{2c_1 c_2} + \frac{c_1^2 x}{c_2}, \quad u_T = (c_1 h)^{-1} \tag{31}$$

otherwise. This solution is also included in the figure.

Nearer the flow front, the solution takes a self-similar form given by

$$\begin{aligned} &h = \delta = \Delta(t) H(\eta), \quad q = Q(\eta), \\ &\eta = \frac{x + x_0}{\Delta}, \quad x_0 = \frac{3c_2 - c_1}{2c_1 c_2}, \quad \Delta = x_f + x_0, \end{aligned} \tag{32}$$

where $x = x_f(t)$ denotes the fluid edge[8]. Equations (28)–(29) become

$$\lambda(H - \eta H') + Q' = 0, \tag{33}$$

$$-\lambda \eta Q' + \left(\frac{c_2 Q^2}{c_1^2 H}\right)' = -\frac{Q}{H^2} \tag{34}$$

where

$$\Delta\dot{\Delta} = \lambda, \quad \text{or} \quad x_f = \Delta - x_0 = \sqrt{x_0^2 + 2\lambda t} - x_0 \tag{35}$$

(using $x_f = 0$ at $t = 0$). The solution must satisfy

$$Q \sim \lambda H \sim c_1 \sqrt{\frac{2\lambda(1-\eta)}{c_2 - c_1^2}}, \quad \text{for} \quad \eta \to 1, \tag{36}$$

and match to the steady flow behind,

$$Q \to 1 \qquad \& \qquad H \to \frac{c_1^2}{c_2}\eta, \quad \text{as} \quad \eta \ll 1. \tag{37}$$

We may solve (33)-(37) approximately by noting that if the front region is relatively narrow, $Q' \to 0$ unless η is close to 1. Then we may crudely solve (33) by taking

$$H \approx \frac{c_1^2}{c_2}\eta Q \qquad \& \qquad \lambda \approx \frac{c_2}{c_1^2}, \tag{38}$$

which automatically incorporates a pair of the boundary and matching conditions. A similar approximation of equation (34) then gives

$$-\frac{Q'}{\eta} + \left(\frac{c_2 Q}{c_1^2 \eta}\right)' \approx -\frac{c_2}{c_1^3 \eta^2 Q}, \tag{39}$$

furnishing

$$Q \approx \sqrt{1 - \eta^{2c_2/(c_2 - c_1^2)}}. \tag{40}$$

The self-similar solution extracted from the numerical computation of the initial-value problem is illustrated in figure 2, and compared to a direct construction from (33)-(37), and the approximation in (40). As noted by Hogg & Pritchard[8], the system in (33)-(37) admits solutions that are continuous in η but suffer a jump in derivative. Indeed, the solution computed and shown in figure 2 has a discontinuous derivative for $\eta \approx 0.808$, where the flux abruptly switches from a declining function at larger η to $Q = 1$. This switch indicates that there is only a relatively narrow self-similar region, which underscores the approximation leading to (40).

Note that, as the film thickens, gravity is likely to become more significant (Hogg & Pritchard[8]). Similarly, surface tension may well play a role if the film develops abrupt changes in depth (as for some of the solutions reported below). In the interest of simplicity, we have ignored both effects in the current paper, although they could be straightforwardly built into the modeling framework. The importance of these effects in practice can be gauged by estimating the Froude number $V_{_J}/\sqrt{gd}$ and Weber number $\rho {V_{_J}}^2 d/\sigma$, where g is the gravitational acceleration and σ is the surface tension.

B. Line source with a moving wall ($x_s \to 0$, $u_{_W} \neq 0$)

A generalization of Watson's problem is to allow the line source at $x = 0$ (with $h(0,t) = 1$, $\delta(0,t) = 0$ and $q(0,t) = \pm 1 - u_{_W}$) to launch fluid above a moving wall.

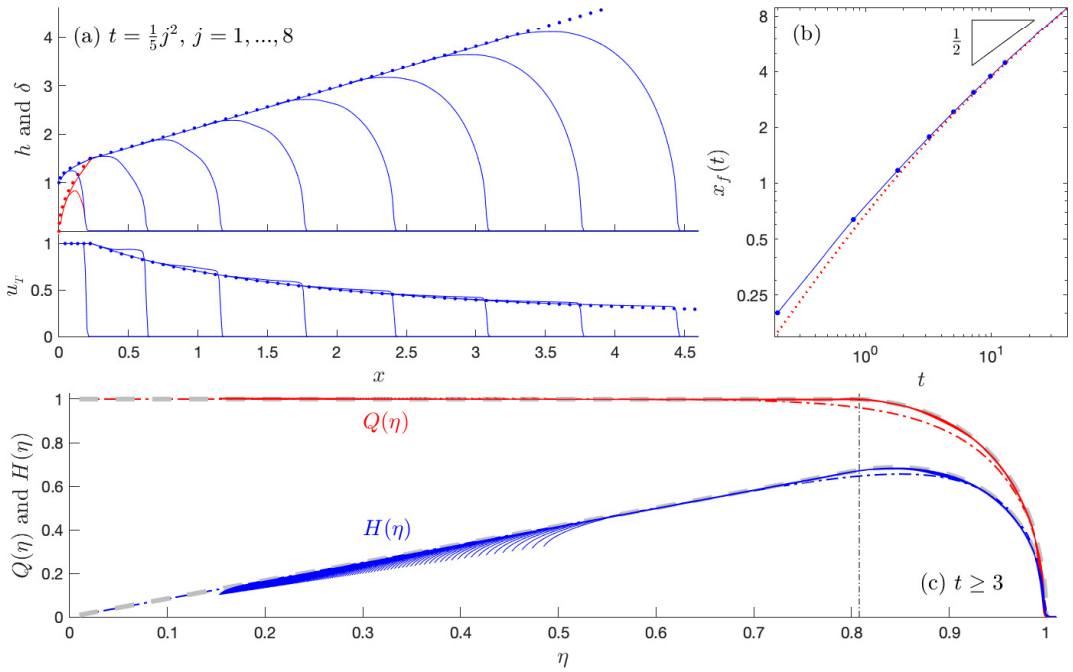

FIG. 2. Numerical solution for a stationary wall ($u_W = 0$, $x > 0$) computed imposing a flux and depth of $q = h = 1$ at $x = 0$. (a) shows snaphosts of h, δ and u_T at the times indicated. The dots show the steady-state solution. The time series of the position of the fluid edge $x_f(t)$ is plotted in (b), along with the prediction in (35) (dotted). In panel (c), the numerical solutions for $t \geq 3$ (each spaced by 0.2 time units) are replotted, scaling variables according to the similarity solution; the thicker dashed grey lines show the numerical solution of (33)-(37) (which gives $\lambda \approx 1.3$), and the dot-dashed lines indicate the approximation given by (40). The vertical line at $\eta \approx 0.808$ locates where the self-similar solution has a jump in derivative.

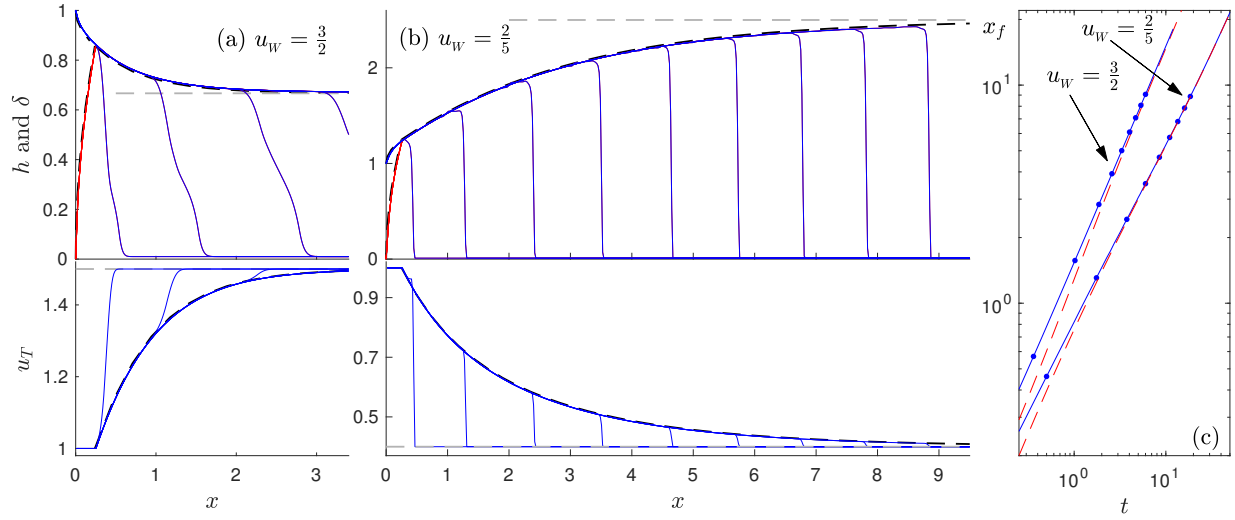

FIG. 3. Numerical solutions for a line source above a wall moving in the same direction ($u_W \neq 0$, $x > 0$). Solutions for (a) $u_W = \frac{3}{2}$ and (b) $\frac{2}{5}$ are presented, plotting snapshots of $h(x,t)$ (blue) and $\delta(x,t)$ (red) above, and $u_T(x,t)$ below. Panel (c) shows time series of $x_f(t)$. The times of the snapshots in (a,b) are indicated by the dots in (c) (only the first four snapshots can be distinguished in (a)). The asymptotes u_W and ${u_W}^{-1}$ are shown by light grey dashed lines in (a); the black dashed lines show the steady-state soutions. The red dashed lines in (c) indicate the flow front $x_f(t)$ predicted by the steady-state solution.

When the wall moves in the direction of the outflow ($u_I = 1$ and $x \geq 0$), the source again generates a travelling fluid step behind which the flow converges to steady state, as illustrated in figure 3. The motion of the wall, however, accelerates (panel (a)) or brakes (panel (b)) the step, which converges to the wall speed at late times, with no self-similar structure appearing nearby.

The case of an outflow above a counter moving wall is

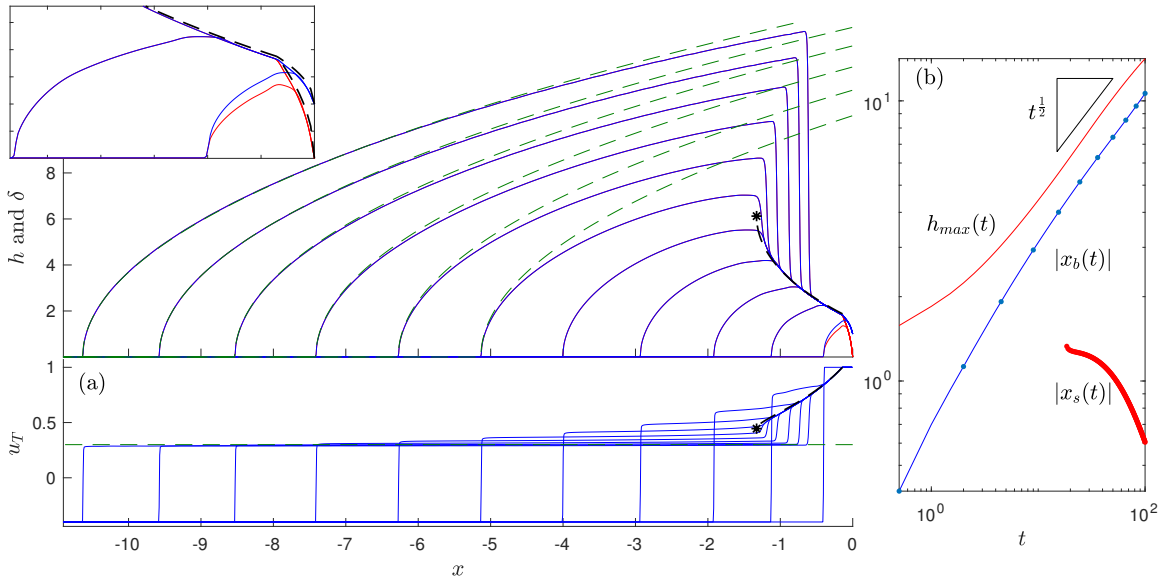

FIG. 4. Numerical solution for a line source above a counter-moving wall ($u_W = 0.4$, $x < 0$). Snapshots of $h(x,t)$, $\delta(x,t)$ and $u_T(x,t)$ are plotted in (a). In (b), we plot time series of $x_b(t)$, $h_{max}(t)$ and the position of the jump $x_s(t)$. The times of the snapshots in (a) are indicated by the dots in (b). The thicker (black) dashed lines in (a) show the steady state solution, which disappears at the position marked by a star; the thinner (green) dashed lines indicate (42) with $u_T = 0.3$. The top left inset shows a magification of the region near the source.

more interesting; see figure 4. In this case, for wall speeds $u_W < (c_1-c_2)/(1+c_2-2c_1)$ (equal to $\frac{2}{3}$ for our parameter settings), another steady solution exists adjacent to the source, satisfying

$$u_W h + q = -1 \quad \text{and} \quad M_x = -\frac{c_1 U}{\delta}. \tag{41}$$

However, this solution terminates a finite distance from the source once the incoming momentum flux becomes unable to balance the net drag on the current. In the initial-value problem (see figure 4), the consequence is that a widening step propagates out from the source, initially leaving behind the steady state. But once the step moves past the termination point of the steady solution, a jump forms instead that then propagates back towards the source. This feature is the analogue of the hydraulic jump in Watson's problem. Unlike Watson's jump, however, which is prompted by the presence of an existing steady flow in the far field, the jump here is induced by the backflow created by the motion of the wall.

To the left of the jump, the fluid layer deepens with time (allowing the momentum flux to counter the net drag), with the surface velocity becoming almost spatially constant at late times. The latter feature is characteristic of an approach to a travelling-wave solution with

$$q \approx c_1 U h \approx (\dot{x}_f - u_W)h,$$
$$h \approx \sqrt{\frac{2c_1(x-x_f)}{U(c_2-c_1^2)}} \tag{42}$$

(since $h = \delta$), which gives a convenient approximation to the form of the solution beyond the jump; see figure 4(a), The flow front advances roughly as $t^{\frac{1}{2}}$ at this stage (figure 4(b)), but once the jump reaches $x = 0$, it interferes with the source conditions and the solutions no longer maintain constant flux, leading us to conclude the computation.

With faster wall speeds, $u_W > (c_1 - c_2)/(1 + c_2 - 2c_1)$, no steady solution exists anywhere. In the initial-value problem with such wall speeds, fluid immediately begins to deepens at the source, creating a jump there that again interferes with the source conditions. The cure for this problematic behaviour is to permit a flux back across the source, which is accounted for in the full jet problem, considered next.

IV. JETS

A. Convergence to steady states for $u_W > 2$

Turning now to the full jet problem (with a finite impact zone and computational domain $-L_1 < x < L_2$), figure 5 shows a sample computation with $u_w = 3$ and $x_s = \frac{1}{8}$. The computation kicks off from a square initial condition with unit depth under the jet, so that $h(x,0) = h_\infty + \Theta(x_s - |x|)$ and $q(x,0) = 0$. The fluid spreads sideways (in the positive and negative x-directions) and deepens, fed by the incoming slot jet. The right-hand edge travels swiftly out of the computational domain, following a similar pattern to that seen for a line source on a wall moving in the flow direction with $u_W > 1$ (§III B and figure 3): the fluid layer thins with distance and the edge accelerates up to the wall

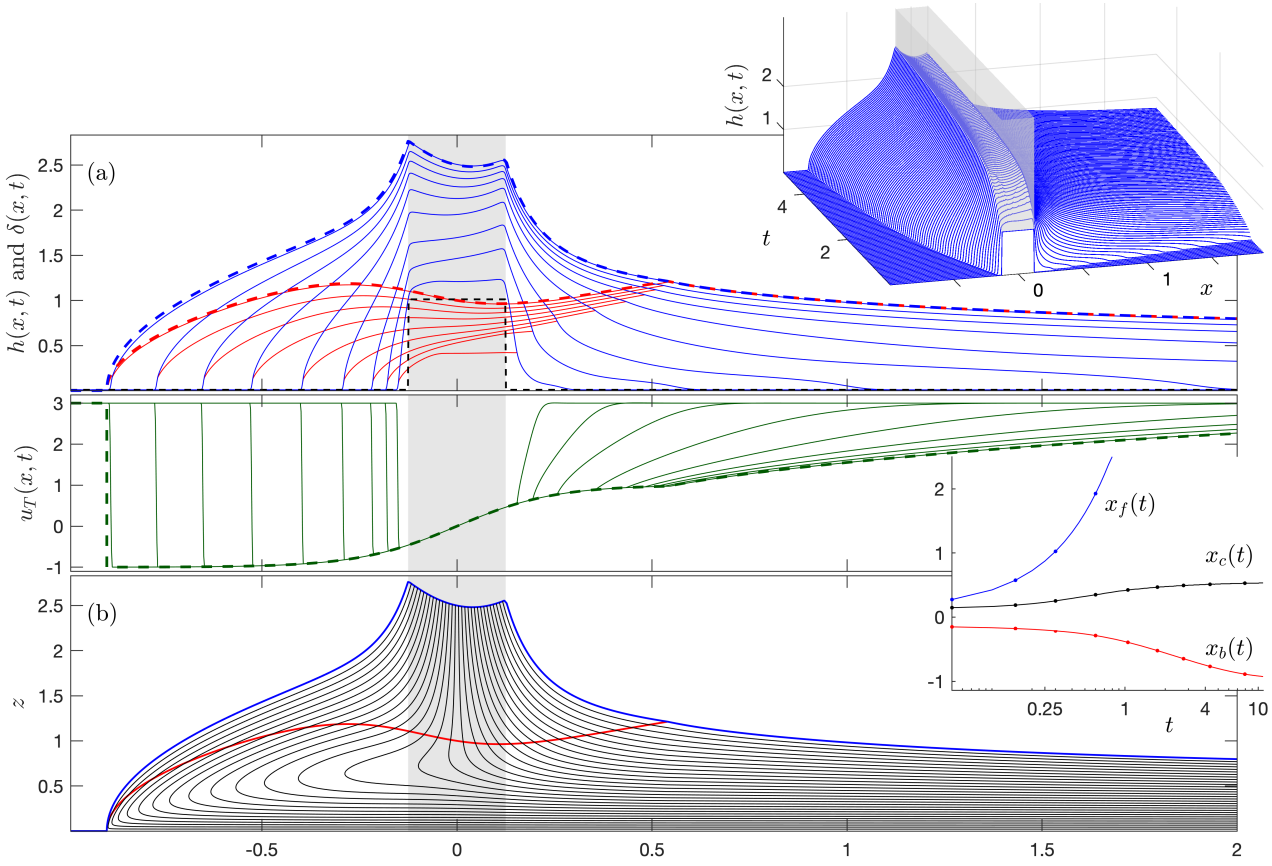

FIG. 5. Numerical solution to the initial-value for a jet with $u_W = 3$ and $x_s = \frac{1}{8}$, launched from the initial condition, $h(x,0) = h_\infty + \Theta(x_s - |x|)$ and $\delta(x,0) = 0$. Panel (a) shows snapshots of h, δ and u_T; the times of the snapshots are indicated in the lower inset, which plots the time series of the front and back edges, $x_f(t)$ and $x_b(t)$, and the position where the boundary layer consumes the entire film, $x_c(t)$. The dashed lines in (a) show the initial condition $h(x,0)$ and steady-state solution. The upper inset shows a rendition of the three-dimensional surface $h(x,t)$ (with the edges of the jet shaded grey). Panel (b) shows a selection of steady-state streamlines.

speed. To the left of the impact zone, the fluid slows and the left-hand edge $x = x_b(t)$ eventually brakes to a halt at some position $x_b \to -x_h$. At this stage, the flow reaches steady state within the computational domain. The fluid directed to the left of the jet becomes recirculated around underneath the impact zone, with all the fluid entering the domain exiting through the right-hand edge. The final steady state can be constructed explicitly, as described in Appendix A and also plotted in figure 5.

The recirculation of the final steady state can be observed in the streamline pattern displayed in figure 5(c), which plots level curves of the streamfunction (defined such that $u = \psi_z$ and $w = -\psi_x$),

$$\psi = \begin{cases} u_T z - \frac{1}{3}u_T\delta + \frac{1}{3}u_W\delta, & \delta < z \le h, \\ u_W z + (u_T - u_W)(\delta^{-1}z^2 - \frac{1}{3}\delta^{-2}z^3), & 0 \le z \le \delta. \end{cases} \tag{43}$$

In the final state, $h \neq 1 + \delta$ at the edges of the impact zone, as might be expected if the jet inflow splits equally above $z = \delta(x,t)$ into the two inviscid currents diverted to either side (as sketched in figure 1). Instead, we observe that the underlying recirculated fluid coupled with the finite extent of the impact zone lead to viscous modifications of the incoming flow. Consequently, within the impact zone, a fraction of the streamlines from the jet intersect the level $z = \delta(x,t)$.

A series of steady-state solutions for $x_s = \frac{1}{8}$ and varying u_W is shown in figure 6, and for varying x_s with $u_W = 3$ in figure 7. The first series is limited to wall speeds $u_W > 2$ (Appendix A): when $u_W < 2$, a fully consumed film ($\delta = h$) develops to the left of the impact zone at $u_W = 2$ eliminating any steady solution. The series also terminates at higher wall speeds ($u_W \approx 11.25$) when the left-hand flow front $x = x_b \equiv -x_h$ reaches the lefthand edge of the jet at $x = -x_s$. Note that a bump develops in the free surface to the left of the impact zone for the smaller wall speeds shown in figure 6, a feature connected to the development of an underlying eddy in the flow pattern (see the inset plot of the flow pattern for $u_W = 2$). Also, the solutions with $u_W = 10$ and 11.2 develop a jump in depth at the position where δ meets h (Appendix A).

In figure 7, the series of solutions at fixed u_W show

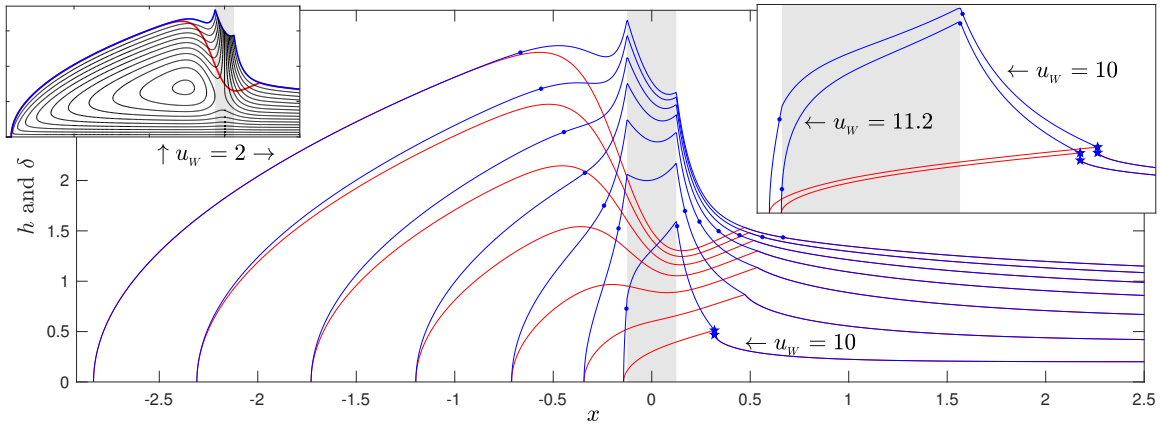

FIG. 6. Steady state solutions for $x_s = \frac{1}{8}$ and $u_W = 2$, 2.125, 2.333, 2.666, 3.333, 5 and 10. The insets show the flow pattern for $u_W = 2$ (left) and the details of the solution with $u_W = 10$ (right), along with another for $u_W = 11.2$. The stars indicate the jump in h arising for $u_W = 10$ and 11.2; the dots show the depths h_R and h_L where $x = \pm\frac{1}{5}(x_h + 4x_s)$.

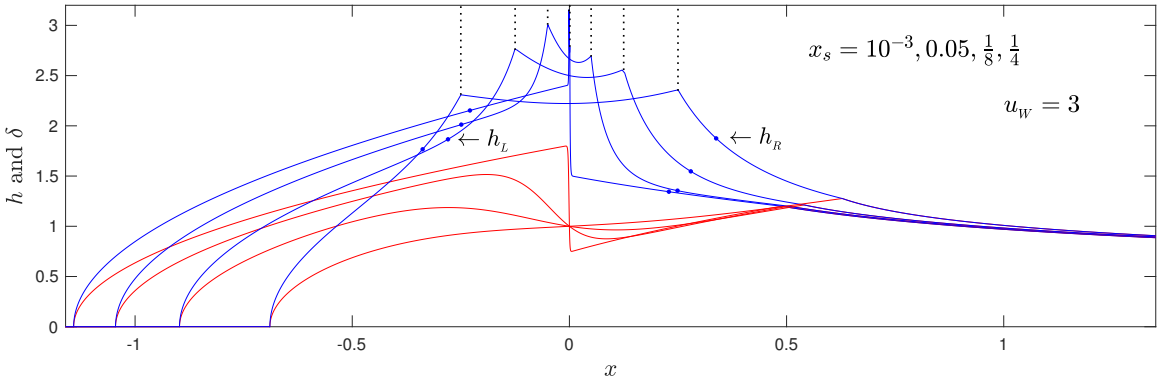

FIG. 7. Steady solutions for $u_W = 3$ and the values of x_s indicated. The dots again show the depths h_R and h_L where $x = \pm\frac{1}{5}(x_h + 4x_s)$.

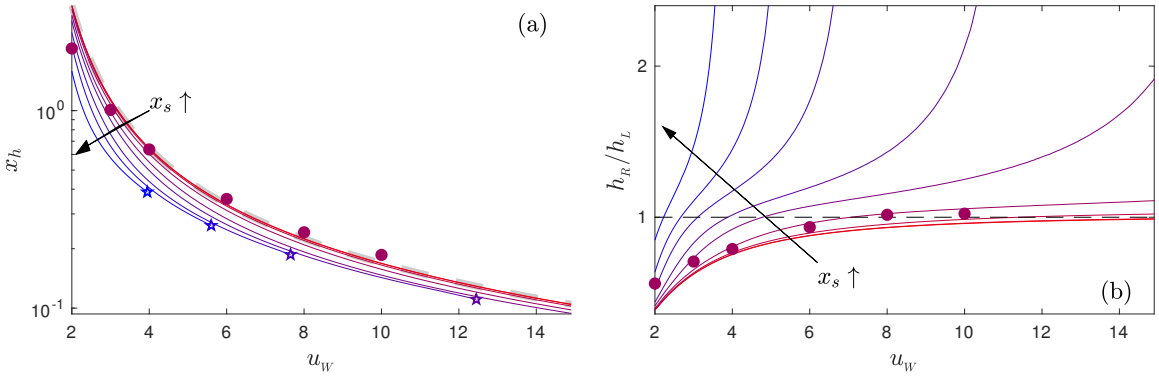

FIG. 8. (a) Heel lengths, x_h, and (b) the depth ratio, h_R/h_L, against wall speed u_W for $x_s = 10^{-4}$, 10^{-3}, 10^{-2}, 0.0336, 0.08, $\frac{1}{8}$, 0.2, 0.275 and 0.4 (coloured from red to blue). In (a) the stars indicate where the heel meets the impact zone, and the gray dashed line shows (44). The filled circles show results from the numerical simulations reported in §V, all for $x_s = 0.0336$.

the convergence to a solution with jumps in h and δ as $x_s \to 0$. The limiting discontinuous solution is explored further in Appendix A, where the jump across the impact zone is rationalized in terms of the net force balance over this region. For wider impact zones, we gauge the left-right asymmetry in the film depths by recording the ratio h_R/h_L, where h_R and h_L are the local depths where $x = \pm\frac{1}{5}(x_h + 4x_s)$ and x_h is the length of the heel (*i.e.* at positions outside the impact zone, by a fraction of the heel; *cf.* figures 6 and 7). Figure 8 shows how the heel

lengths and depth ratio $h_{_R}/h_{_L}$ depends on $u_{_W}$ for several values of x_s. The heel lengths do not show much variation with jet width x_s, aside from where they intersect the impact zone, leading to the disappearance of the solution (as indicated by the stars). The depth ratio $h_{_R}/h_{_L}$ is mostly smaller than unity, reflecting the build-up of fluid in the heel; only when the heel approaches the impact zone or at the very highest wall speeds is $h_{_R} > h_{_L}$.

In Appendix A, for $x_s \to 0$, we derive the relation

$$x_h = \frac{u_{_W}(1+c_2-2c_1)}{2c_1(1-c_1)^2(u_{_W}+1)^2} \times \left[1 - \frac{c_1-c_2}{u_{_W}(1+c_2-2c_1)}\right]^{\frac{2-c_2-c_1}{c_2-c_1}}. \tag{44}$$

This limit is also included in figure 8, and provides a fair approximation for the smaller jet widths presented ($x_s < 0.1$). Note that, in dimensional units, the heel length is

$$\frac{c_1 V_{_J} d^2}{4c_0\nu} x_h(u_{_W}, x_s) \equiv \tfrac{1}{2} d\,\mathrm{Re}_{_J} \frac{c_1}{2c_0} x_h\left(\frac{V_{_W}}{V_{_J}}, \frac{2c_0}{c_1 \mathrm{Re}_{_J}}\right).$$

B. Unsteady states for $u_{_W} < 2$

Solutions illustrating the dynamics for lower $u_{_W}$ are displayed in figure 9. With $u_{_W} = 0$, the fluid diverges symmetrically from the impact zone, with the boundary layer quickly consuming the film. The presence of a finite impact zone does not, however, lead to a very different solution structure to that seen for the line source considered in III A; self-similar regions near the left and right fluid fronts advance roughly as $t^{\frac{1}{2}}$ (the snapshots are spaced equally in t^2), with the flow behind converging to a steady state in which the flow depth increases linearly with position.

When $u_{_W} \neq 0$, and as for a line source directed with the wall (§III B), the fluid to the right of the impact zone either slows ($u_{_W} < 1$) or accelerates up ($u_{_W} > 1$) to the wall speed, deepening or thinning the fluid layer, repectively. For $u_{_W} = 0.4$, the left-going flow follows the pattern found earlier for a line source on a counter-moving wall (§III B and figure 4): the flow converges initially to a steady state (with finite left-going flux). But that steady state then terminates, and the solution of the initial-value problem then develops a jump that travels back towards the impact zone. All the while, fluid continues to deepen and move left, with the solution converging towards the travelling-wave form

$$u_{_T} \sim constant \qquad \& \qquad h^2 \sim \frac{2c_1(x-x_b)}{U(c_2-c_1^2)}, \tag{45}$$

analogous to (42).

With $u_{_W} > \frac{2}{3}$, and no steady state to the left of the impact zone, the solutions of the initial-value problem deepen immediately in $x < -x_s$, developing an abrupt step that enters the impact zone. The step regulates the fluxes delivered to the left and right, which then drift with time. For the solution with $u_{_W} = 1.5$ shown in figure 9(c,e), the slow increase in the rightward flux leads to a gradual deepening of the film in $x > x_s$.

C. Alternative steady states

A more curious result is that the solutions shown in figures 5 and 6 are not the only ones possible for the parameters settings chosen: if, for example, we launch the computation in figure 5 with $u_{_W} = 3$ from the pre-wetted film alone (*i.e.* $h = h_\infty$ and $q = 0$ at $t = 0$), a different steady state develops in which the layer is fully consumed by the boundary layer everywhere, as shown in figure 10(a). With this initial condition, the fluid becomes swept leftwards immediately and no embedded boundary layer ever develops. Instead, the solution converges to a different steady state without a heel, that can again be constructed directly, as outlined in Appendix A.

The alternative steady states exist over a wider range of walls speeds to those with heels. In figure 10(b), we plot the alternative solutions corresponding to those shown earlier in figure 6 for $x_s = \frac{1}{8}$ and a selection of values of u_w. For this value of x_s, the heel-less states exist down to wall speeds just below $u_{_W} = 1$ (see Appendix A). They are also the steady states reached whenever initial-value computations are kicked off from the pre-wetted film alone for all $u_w > 1.5$ (for smaller wall speeds, these initial-value problems again become time dependent).

It also turns out that once the steady states with heels are lost at higher $u_{_W}$, the initial-value computations launched from the initial conditions, $h(x,0) = h_\infty + \Theta(x_x - |x|)$ and $\delta(x,0) = 0$, approach the heel-less steady state as well. In other words, when the heel enters the impact zone, there is a sudden switch of the steady state. Although it seems plausible that heel-less steady states arise at higher wall speeds if the impact zone has finite size, the persistence of these states to low wall speeds sounds less realistic. It is possible that these solutions are an artefact of the approximations made in the reduction to the shallow-layer model, and, in particular, our relatively crude treatment of the impact zone.

V. COMPARISON TO NUMERICAL SIMULATIONS

We compare the predictions of the shallow-layer theory with computations using Ansys FLUENT software. This code employs the volume-of-fluid method to locate the interface between the fluid descending in the jet and a second ambient fluid with the physical properties of air. The computational domain, in the dimensionless units of §II C is a $192x_s \times 16$ rectangle, extending from $-120x_s$ on the left to $x = 72x_s$ on the right. Boundary conditions of no slip are imposed along $z = 0$, and "pressure-

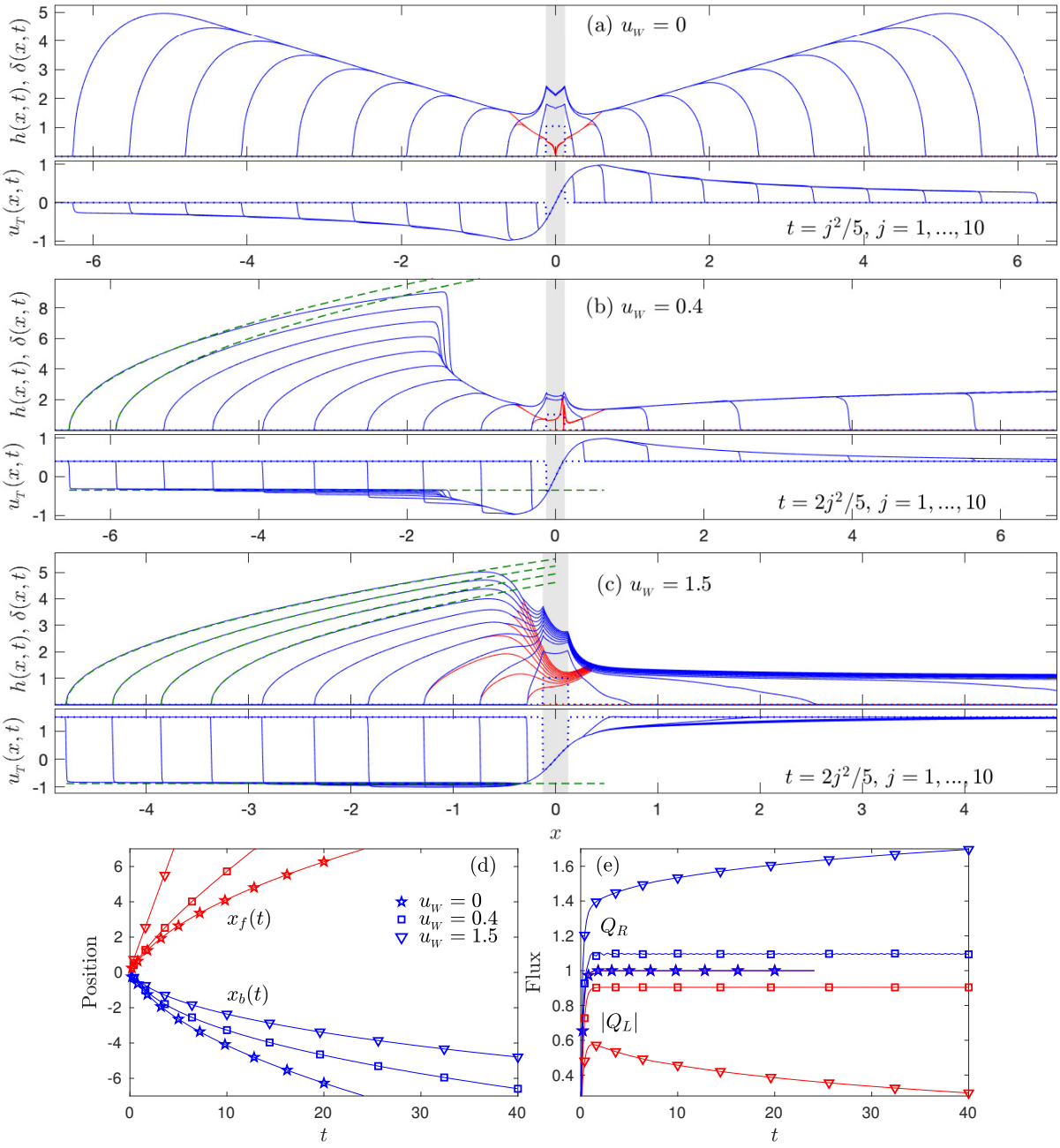

FIG. 9. Shallow layer solutions, launched from the initial condition, $h(x,0) = h_\infty + \Theta(x_s - |x|)$ and $\delta(x,0) = 0$ (indicated by dotted lines), showing snaphots of h, δ and u_T at the values of u_W and times indicated; $x_s = \frac{1}{8}$. For $u_w > 0$, the dashed lines show a fitted constant value for u_T and the resulting approximation for h in (45). The lower panels show corresponding time series of (d) the fluid edges, $x_f(t)$ and $x_b(t)$, and (e) the leftward and rightward fluxes, $|Q_L|$ and Q_R, at the edges of the jet ($x = \pm x_s$). The symbols indicate the times of the snapshots in (a)-(c).

outlet" conditions are prescribed along the vertical side walls and the top, except where the jet enters the domain. For the latter, at $z = 16$ and $-x_s \le x \le x_s$, we set $(u, w) = (0, -1)$. The computations are commenced from the moment that the jet reaches the moving wall; *i.e.* such that there is an initial column of liquid occupying $-x_s \le x \le x_s$ and $0 < z < 16$ with velocity $(u, w) = (0, -1)$. Evolution is continued until a steady state is reached, if one arises, or until the main features of the dynamics are evident.[17]

Figure 11 displays the steady state reached for a sample numerical solution with $\mathrm{Re}_J = 180$ and $u_W = 3$, which corresponds to using the shallow-layer model with a dimensionless jet width of $x_s = 0.0336$. The top panel of the figure displays the pressure distribution, interface position and sample streamlines from the two-

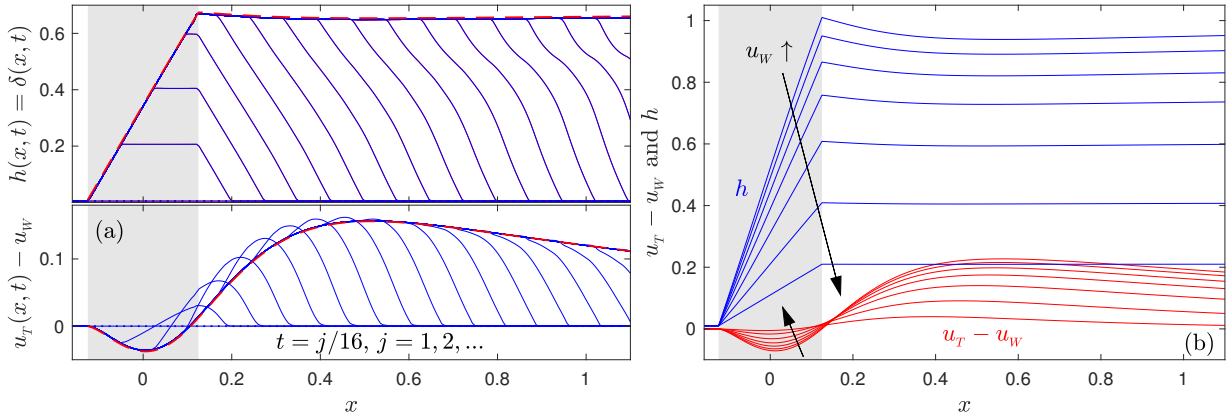

FIG. 10. (a) The Shallow layer solution launched from the pre-wetted film alone ($h(x,0)=h_\infty$ and $u_T(x,0)=u_W$) with $x_s=\frac{1}{8}$ and $u_w=3$, showing snaphots of $h=\delta$ and u_T-u_W at the times indicated. The dashed lines show the steady-state solution. More steady state solutions are shown in (b) for the same values of u_W as presented in figure 6.

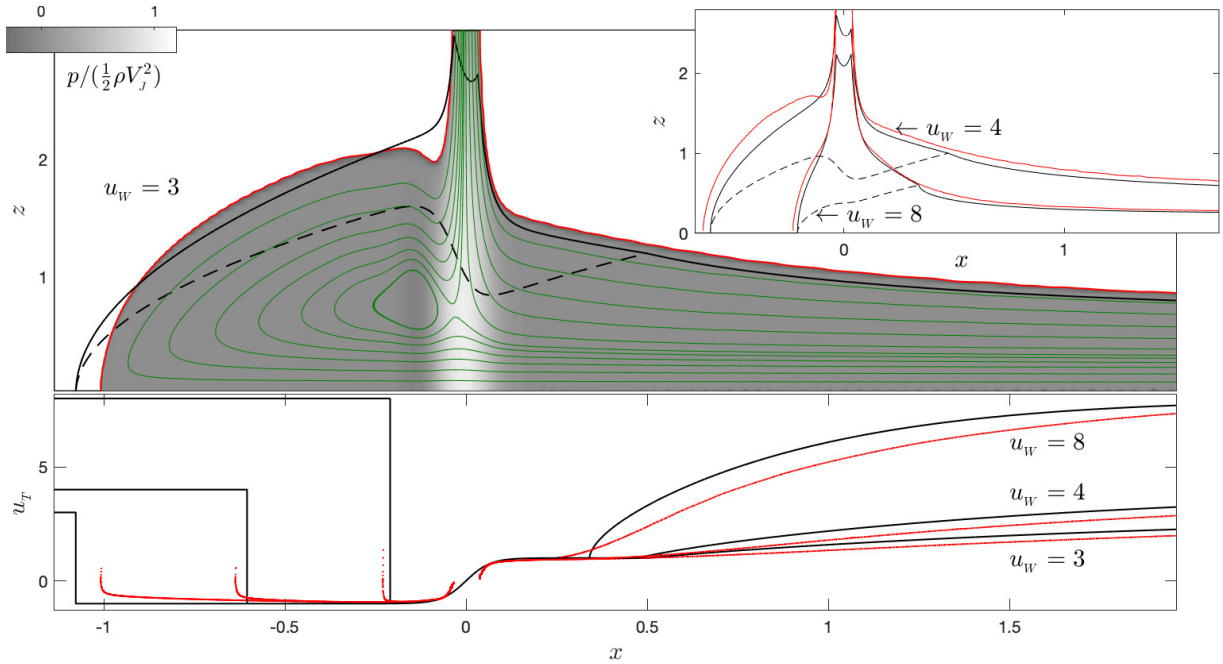

FIG. 11. Two-dimensional numerical solution for $u_W=3$ and $\mathrm{Re}_J=180$. The upper panel shows the interface (red line), pressure distribution (grey shading, scaled by $\frac{1}{2}\rho V_J{}^2$) and sample streamlines (thinner green lines). The $(x,z)-$spatial coordinates are scaled with L and $\frac{1}{2}d$, respectively, as in the shallow layer theory. The lower panel shows the horizontal speed at the interface (red). The thick black lines show h (solid), δ (dashed) and u_T (solid, lower panel) for the shallow-layer theory ($x_s\equiv d/(2L)=0.0336$). Also included in this panel are two more solutions with $u_W=4$ and 8 (again with $\mathrm{Re}_J=180$); the corresponding interfaces, $h(x)$ and $\delta(x)$ are displayed in the overlaid panel at the top right.

dimensional numerical solution; the lower panel shows the horizontal velocity along the interface. As expected, the pressure is largely uniform, and elevated only over the impact zone. The plots also show the predictions of the shallow-layer theory for levels $z=h(x)$ and $z=\delta(x)$ and the surface velocity $u_T(x)$, in the steady, heeled state at this wall speed. An inset to the figure shows a similar comparison of the numerically computed interface with $h(x)$ for two other values of u_W; data for heel lengths and depth ratios from more simulations are included in figure 8 (all with $x_s=0.0336$, or $\mathrm{Re}_J=180$).

Overall, the comparison between the numerical simulations and the shallow-layer model is satisfying, though not quantitative: both simulations and model predict steady states with heels, the profile of free surfaces are largely similar, and the heel lengths and depth ratios match fairly well. However, the finer features of the flow pattern and free surface profile are not reproduced. For example, the bump on the free surface of the heel (and the corresponding eddy underneath) persists to higher

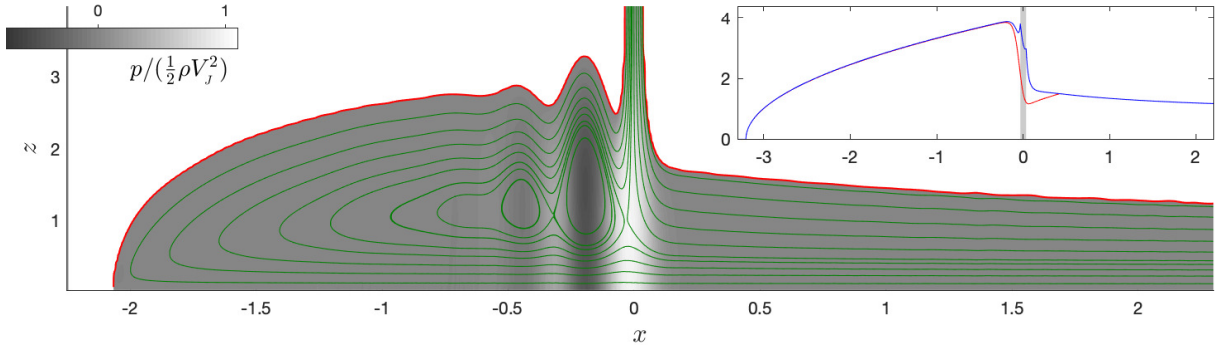

FIG. 12. Two-dimensional numerical solution for $u_w = 2$ and $\mathrm{Re}_j = 180$, showing the final (steady) interface, pressure distribution and sample streamlines. The inset shows the limiting shallow-layer solution for $u_w \to 2$ and $x_s = 0.0336$. The pressure distribution, streamlines and interface location follow the convention in figure 11.

wall speeds in the numerical solutions than in the model. In the simulation for $u_w = 2$, there are, in fact, multiple bumps, each associated with noticeable pressure variations (see figure 12). For higher u_w, there is also little sign of a sharp change in surface slope near the point to the right of the impact zone where the surface velocity begins to decrease below V_j (*i.e.* where $\delta(x,t)$ reaches $h(x,t)$). These discrepancies may result because such surface features do not conform to the shallow-layer scalings.

Lowering the wall speed in the numerical computations also demonstrates a loss of the steady, heeled solutions (for $\mathrm{Re}_j = 180$). In the computations, the solution becomes unsteady between $u_w = \frac{3}{2}$ and $u_w = 2$, in qualitative, but not quantitative, agreement with the predictions of the shallow-layer theory (at $u_w = 2$, the theory also overpredicts the heel length by about fifty percent; figure 12). Figure 13 compares results from the simulations with the predictions of the shallow-layer theory for three walls speeds $u_w < 2$ (*cf.* figure 9). The simulations all show how the spreading film continues to advance and deepen to the left of the jet, as predicted by the model. However, the heels for $u_w > 0$ again show undulations just to the left of the jet, degrading the comparison between model and simulation. Worse, short-wavelength disturbances also develop to the left at late times in the simulations, suggestive of a shear instability, that rapidly breaks up the film (the incipient instability is visible on the final interfaces plotted in figure 13(a,c)). No such features appear when the wall is stationary (figure 13(e,f)), and, indeed, the model is relatively successful in reproducing the transient dynamics seen in the simulations for this case. In fact, finer tuning of the constants, c_j, could clearly be made to bring the slope of the steady profiles reached behind the advancing fluid front in figure 13(e) into agreement (see (31), and the definition of the length-scale L in (24) used to scale the simulation data).

Similarly, as predicted by the shallow-layer theory, the steady, heeled states again disappear in the numerical computations at higher wall speeds. This occurs for u_w between 10 and 12 in the simulations, at this value of Reynolds number (or x_s), far lower than the limit arising in the model (which is just above $u_w = 40$). Moreover, rather than converging to a different, unheeled steady state, the solution in the numerical computations becomes time-dependent, with small-scale features developing from the impacting jet prompting splash-like dynamics. Evidently, the full two-dimensional problem features short-wavelength structures that cannot be captured by our shallow-layer approximation.

VI. DISCUSSION

In this paper, we have constructed a shallow-layer theory for the spreading films created by the impact of a jet on a moving surface. The construction follows the classical von Karman-Pohlhausen averaging technique, but allows the flow to be unsteady and incorporates the incoming jet by including suitable sources of mass and (horizontal) momentum. Once the viscous boundary layer consumes the entire film, the theory becomes equivalent to a shallow-water model with viscous drag (*i.e.* a St Venant model with bottom friction stemming from the viscous shear stress, as dictated by the prescribed velocity profile across the film), although we neglected gravity in the present study.

We used the shallow-layer theory to explore the effect of a varying wall speed on the film dynamics, although along the way, we considered two simpler problems acting as building blocks towards the full jet problem. The first of these corresponds to the time-dependent version of the two-dimensional problem considered by Watson[20], ignoring the development of any sudden jumps in depth due to either downstream conditions or gravity. The time-dependent spreading version of Watson's problem features a self-similar development of the fluid's forward edge. The second problem corresponds to a line source (sluice gate) delivering a constant flux onto a wall moving in the same or opposite direction.

In the full jet problem, steady states are found to be possible only provided the ratio of the speeds of the wall

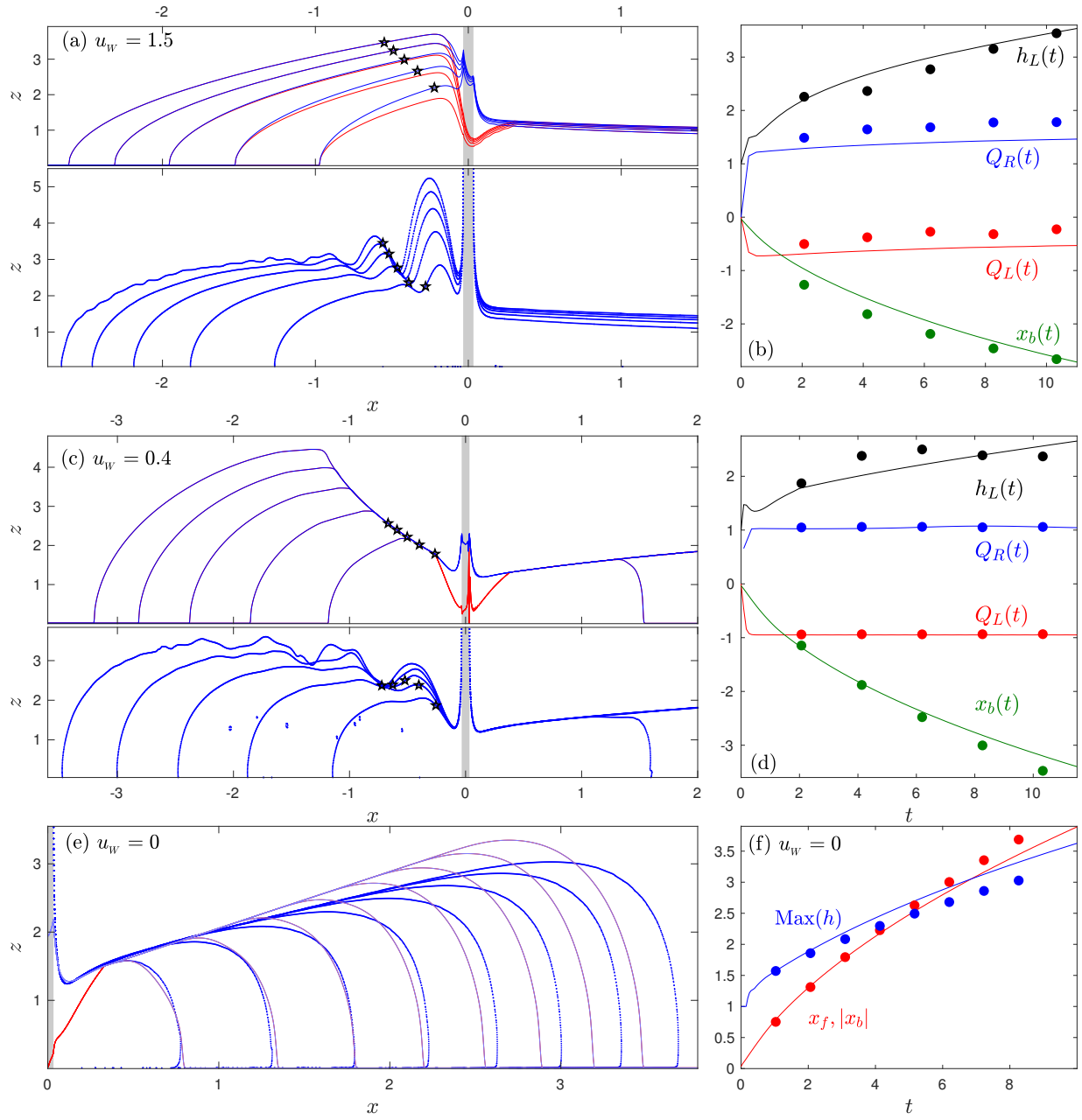

FIG. 13. Comparison of numerical simulations with shallow-layer theory for (a)-(b) $u_W = 1.5$, (c)-(d) $u_W = 0.4$ and (e)-(f) $u_W = 0$, with $\mathrm{Re}_J = 180$ ($x_s = 0.0336$). Plotted in (a,c,e) are snapshots of the interface from the simulations (thicker blue), then $\delta(x,t)$ and $h(x,t)$ for the shallow-layer theory (red and lighter blue). Panels (b,d) show time series of the leftward and rightward fluxes, $Q_L(t)$ and $Q_R(t)$, at $x = \pm 2x_s$, the position of the lefthand fluid edge $x_b(t)$, and the depth $h_L(t)$ at $x = \frac{1}{5}x_b - \frac{4}{5}x_s$ (indicated by the stars in (a,c)). Panel (f) shows $x_b(t)$ and the maximum film depth away from the impact zone; in (e), we show only the right-half of the domain, the solution being left-right symmetric about the origin. For (b,d,f), the circles show data from the simulations (at the times of the snapshots in (a,c,e)); the lines are from the shallow-layer theory. For $u_W = 0.4$ in (c), the volume-of-fluid simulations feature the entrainment of small bubbles of the ambient air.

and jet (u_W, in our dimensionless notation) exceeds two. These steady states feature a distinctive "heel" in which the fluid directed against the wall's motion becomes recirculated back underneath the jet, to leave no net flux to that side of the jet (*cf.* Miyamoto & Katagiri[15]). Approaching the limit $u_W = 2$ (from above), the flow in the heel develops a distinctive bump in the free surface corresponding to an underlying recirculating eddy in the flow pattern. The length of the heel never exceeds $0.245d\mathrm{Re}_J$, where d and $\mathrm{Re}_J = dV_J/\nu$ are the jet width and Reynolds number (*cf.* figure 8 and §IV A).

Below the limit $u_W = 2$, the wall motion is insufficient

to stop the fluid from continually flowing away from the impact zone. Nevertheless, the further the fluid propagates away from the jet, the more viscous drag is exerted by the moving wall, which prevents the flow from converging to s steady state beyond some distance from the jet. Thereafter, the fluid begins to pile up and form a jump that propagates back towards the jet. Although we have not explored the subsequent evolution in any detail, the fluxes diverted to the left and right become modified when the step reaches the impact zone, leaving a time-dependent state in which the fluxes drift with time and fluid continues to make progress against the wall.

The steady states for $u_{_W} > 2$ can also disappear if the velocity ratio is increased too much and the end of the heel migrates into the impact zone. The heel then disappears, leaving a different steady solution in which the film is fully consumed by the viscous boundary layer everywhere and fluid nowhere flows against the motion of the wall. In the shallow-layer theory, the transition between the two steady states is abrupt, with the alternative steady state existing even at lower velocity ratios.

We have also compared the predictions of the shallow-layer theory with numerical computations of the full two-dimensional problem. Although the agreement is not quantitative, the theory is qualitatively successful in predicting the overall structure of the steady states and their disappearance at both low and high velocity ratios. However, the dynamics observed once the steady states are lost is more complicated than found in the model.

Appendix A: Steady states

If the film reaches a steady state with all the fluid eventually being redirected to flow in the direction of the moving wall, then

$$Q(x) = u_{_W} h + q = \begin{cases} 0, & x < -x_s, \\ (x + x_s)/x_s, & -x_s < x < x_s, \\ 2, & x_s < x, \end{cases} \tag{A1}$$

and

$$\frac{\mathrm{d}M}{\mathrm{d}x} = h u_{_I} u_{_I}{}' + US - \frac{c_1 U}{\delta}. \tag{A2}$$

Where $\delta < h$, the flux condition (A1), indicates that

$$U(1 - c_1)\delta = u_{_I} h - Q. \tag{A3}$$

But at $x = 0$, $Q = 1$ and $u_{_I} = 0$, implying that

$$\delta(0) = [u_{_W}(1 - c_1)]^{-1}. \tag{A4}$$

This condition can be used to initiate a numerical integration of (A2) over the impact zone.

To the left of the impact zone, a solution to (A1)-(A2) cannot be found if $\delta = h$. If $\delta < h$, on the other hand, (A2)-(A3) imply that

$$\begin{aligned} \delta^2 &= [\delta(x_{_L})]^2 + \frac{2c_1(x - x_{_L})}{u_{_W}(1 + c_2 - 2c_1) - c_1 + c_2}, \\ h &= (1 + u_{_W})(1 - c_1)\delta, \end{aligned} \tag{A5}$$

taking $u_{_I} = -1$ and $S = 0$ in (A2) for $x < x_{_L}$, where $x = x_{_L}$ denotes the lefthand edge of the impact zone. Thus, provided $u_{_W}(1 + c_2 - 2c_1) > c_1 - c_2$ and $(1 + u_{_W})(1 - c_1) > 1$, the fluid depth decreases to zero at a finite position given by

$$x_b = x_{_L} - \frac{[\delta(x_{_L})]^2}{2c_1}[u_{_W}(1 + c_2 - 2c_1) - c_1 + c_2], \tag{A6}$$

with the boundary layer persisting up to that edge. The constraints on $u_{_W}$ translate to $u_{_W} > 2$ for $c_1 = \frac{2}{3}$ and $c_2 = \frac{8}{15}$. For $u_{_W} < 2$, no steady state with $\delta < h$ to the left of the impact zone is possible,

To the right of the impact zone, the boundary layer solution with $\delta < h$ is

$$\begin{aligned} \delta^2 &= [\delta(x_{_R})]^2 + \frac{2c_1(x - x_{_R})}{c_1 - c_2 + u_{_W}(1 + c_2 - 2c_1)}, \\ h &= 2 + (1 - u_{_W})(1 - c_1)\delta, \end{aligned} \tag{A7}$$

where $x_{_R}$ is the righthand edge of the impact zone. That is, the boundary layer thickens with distance from the impact zone until it consumes the fluid layer with

$$h = \delta = \frac{2}{c_1 + u_{_W}(1 - c_1)}. \tag{A8}$$

Thereafter, the fully developed shear flow satisfies

$$q_x = -\frac{c_1^2 q}{4c_1^2 + (4 - q)q(c_2 - c_1^2)}, \quad h = \frac{2 - q}{u_{_W}}. \tag{A9}$$

Note that q_x diverges for $q = 2 + 2\sqrt{c_2/(c_2 - c_1^2)} \approx 6.899$, which can arise for solutions at larger values of $u_{_W}$. A jump then appears in the solution, as noted in §IV A.

In the limit $x_s \to 0$, the impact zone shrinks to a point, with a jump in depth applying across $x = 0$. For this limit, provided that $h > \delta$, we may discard the final drag term in (A2) and reduce equations (A1)-(A3) to

$$\{U\delta[(c_1 - c_2)u_{_I} + (1 + c_2 - 2c_1)u_{_W}]\}_x = -(1 - c_1)U\delta u_{_I}{}'. \tag{A10}$$

Hence, in view of (A8) and $u_{_W} > 1$,

$$\delta = \frac{1}{(1 - c_1)(u_{_W} - u_{_I})} \left| 1 + \frac{(c_1 - c_2)u_{_I}}{(1 + c_2 - 2c_1)u_{_W}} \right|^{-\frac{(1-c_2)}{(c_1-c_2)}} \tag{A11}$$

Taking $u_{_I} = \pm 1$ now provides the jump in $\delta(x)$ across the impact zone, from which the remainder of the solution can be constructed. Figure 14 compares a solution for $x_s = 10^{-3}$ with the limits implied by (A11). The fine structure over the impact zone is sensitive to the detailed form adopted for the impacting pressure gradient (*i.e.*

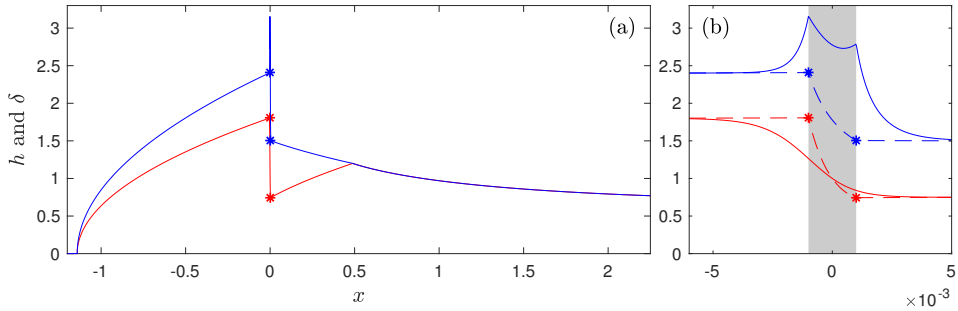

FIG. 14. Steady state solution for $x_s = 10^{-3}$ and $u_W = 3$. The stars indicate the limits predicted by (A11). The full solution is shown in (a); a magnification of the impact zone is plotted in (b), with the dashed lines showing the fine structure of a solution computed with the alternative choice, $u_I = Q - 1$, where $Q(x)$ is given by (A1).

$u_I(x)$), but the jump condition in (A11) is not. This is also illustrated in figure 14, which includes a solution computed using the piece-wise linear ramp $u_I = Q - 1$, where $Q(x)$ is given by (A1).

The jump across the impact zone results from a combination of the mass influx from the jet and the net momentum injection. The latter is given by an integral of the right-hand side of (A2) less the drag term:

$$\mathrm{Lim}_{x_s \to 0} \int_{-x_s}^{x_s} (h u_I u_I{}' + US)\, \mathrm{d}x. \qquad \text{(A12)}$$

A net injection of momentum arises because the impact pressure exerts a net force when there is a jump in depth across the impact zone (first term in (A12). In addition, although the jet provides no net source of momentum in the frame of the inflow, there is nevertheless an injection in the frame of the wall (second term in (A12)).

The alternative steady solutions shown in figure 10(b) are constructed by assuming that $h = \delta$ everywhere and initiating a solution from $x = -x_s$ with $h = q = 0$. Again, as $x_s \to 0$, the impact zone narrows to a point across which the fluid depth jumps. These solutions exist for $u_W > 1$ for all x_s, but disappear for $u_W \approx 0.7$ at $x_s = \frac{1}{8}$, and $u_W \approx 0.92$ for $x_s \to 0$.

[1] R. K. Bhagat and D. I. Wilson, *Flow in the thin film created by a coherent turbulent water jet impinging on a vertical wall*, Chemical Engineering Science, 152 (2016), pp. 606–623.

[2] R. I. Bowles and F. T. Smith, *The standing hydraulic jump: theory, computations and comparisons with experiments*, Journal of Fluid Mechanics, 242 (1992), pp. 145–168.

[3] J. W. M. Bush, J. M. Aristoff, and A. E. Hosoi, *An experimental investigation of the stability of the circular hydraulic jump*, Journal of Fluid Mechanics, 558 (2006), pp. 33–52.

[4] C. Ellegaard, A. E. Hansen, A. Haaning, K. Hansen, A. Marcussen, T. Bohr, J. L. Hansen, and S. Watanabe, *Polygonal hydraulic jumps*, Nonlinearity, 12 (1999), p. 1.

[5] H. Fujimoto, Y. Suzuki, T. Hama, and H. Takuda, *Flow characteristics of circular liquid jet impinging on a moving surface covered with a water film*, ISIJ international, 51 (2011), pp. 1497–1505.

[6] M. Gradeck, A. Kouachi, A. Dani, D. Arnoult, and J. L. Borean, *Experimental and numerical study of the hydraulic jump of an impinging jet on a moving surface*, Experimental thermal and fluid science, 30 (2006), pp. 193–201.

[7] F. J. Higuera, *The hydraulic jump in a viscous laminar flow*, Journal of Fluid Mechanics, 274 (1994), pp. 69–92.

[8] A. J. Hogg and D. Pritchard, *The effects of hydraulic resistance on dam-break and other shallow inertial flows*, Journal of Fluid Mechanics, 501 (2004), pp. 179–212.

[9] R. P. Kate, P. K. Das, and S. Chakraborty, *Hydraulic jumps due to oblique impingement of circular liquid jets on a flat horizontal surface*, Journal of Fluid Mechanics, 573 (2007), pp. 247–263.

[10] J. H. Lienhard, *Liquid jet impingement*, Annual Review of Heat Transfer, 6 (1995).

[11] ———, *Heat transfer by impingement of circular free-surface liquid jets*, in 18th National and 7th ISHMT-ASME, Heat and Mass Transfer Conference, Guwahati, India, 2006.

[12] X. Liu, *Liquid jet impingement on a moving wall*, PhD thesis, University of British Columbia, 2022.

[13] X. Liu, N. J. Balmforth, S. Green, and B. Stoeber, *Impingement of a two-dimensional jet on a moving wall*, In preparation, (2022).

[14] J. Majdalani and L.-J. Xuan, *On the Kármán momentum-integral approach and the Pohlhausen paradox*, Physics of Fluids, 32 (2020), p. 123605.

[15] K. Miyamoto and Y. Katagiri, *Curtain coating*, in Liquid film coating, Springer, 1997, pp. 463–494.

[16] J. B. T. Moulson and S. Green, *Effect of ambient air on liquid jet impingement on a moving substrate*, Physics of Fluids, 25 (2013), p. 102106.

[17] Because no interfacial tension is included and a concentration field is employed to distinguish the two fluids (which diffuses as a result of finite numerical resolution), there is no true interface in these computations. Moreover, the no-slip boundary condition on the moving plane prevents any contact between the moving plane and the fluid from the jet. Instead, a thin finger of ambient fluid unavoidably becomes swept along underneath the spreading shallows films diverted from the jet. This finger becomes too thin to resolve in the computations, leaving an intermediate concentration along the lowest line of grid cells. Mesh refinement studies suggest that the unresolved finger does not problematically affect the numerical solution elsewhere (these studies suggest that, for the steady states, the heel length x_h and the horizontal velocity at select vertical cross sections converge to within a few percent). The finger can also be artificially removed by suitably resetting the concentration field in the lowest grid cells. This device avoids any issues with spatial resolution, at the expense of an apparent violation of mass conservation, but again does not affect the solution elsewhere. Consequently, although the finger reflects a limitation of the computations, it does not therefore appear significant and our plots of the "interface", defined by the level curve of the concentration midway between the two phases, omit that part associated with the finger. More details of the simulations, including the results of mesh convergence studies will be

presented elsewhere[12,13].

[18] B. Scheichl and A. Kluwick, *Laminar spread of a circular liquid jet impinging axially on a rotating disc*, Journal of Fluid Mechanics, 864 (2019), pp. 449–489.

[19] T. Wang, D. Faria, L. J. Stevens, J. S. C. Tan, J. F. Davidson, and D. I. Wilson, *Flow patterns and draining films created by horizontal and inclined coherent water jets impinging on vertical walls*, Chemical Engineering Science, 102 (2013), pp. 585–601.

[20] E. J. Watson, *The radial spread of a liquid jet over a horizontal plane*, Journal of Fluid Mechanics, 20 (1964), pp. 481–499.

[21] D. I. Wilson, H. Köhler, L. Cai, J.-P. Majschak, and J. F. Davidson, *Cleaning of a model food soil from horizontal plates by a moving vertical water jet*, Chemical Engineering Science, 123 (2015), pp. 450–459.

[22] D. A. Zumbrunnen, *Convective heat and mass transfer in the stagnation region of a laminar planar jet impinging on a moving surface*, ASME Journal of Heat Transfer, 113 (1991), pp. 563–570.

[23] D. A. Zumbrunnen, F. P. Incropera, and R. Viskanta, *A laminar boundary layer model of heat transfer due to a nonuniform planar jet impinging on a moving plate*, Wärme-und Stoffübertragung, 27 (1992), pp. 311–319.